AIAA Journal
Vol. 37, No. 1, January 1999

Reynolds-Averaged Navier–Stokes Computations of a Flap-Side-Edge Flowfield

Mehdi R. Khorrami,[*] Bart A. Singer,[†] and Ronald H. Radeztsky Jr.[‡]
High Technology Corporation, Hampton, Virginia 23666

An extensive computational investigation of a generic high-lift configuration comprising a wing and a half-span flap reveals details of the mean flowfield for flap deflections of 29 and 39 deg. The computational effort involves solutions of the thin-layer form of the Reynolds-averaged Navier–Stokes equations. For both flap deflections, the steady results show the presence of a dual-vortex system: a strong vortex forming on the lower portion of the flap side edge and a weaker one forming near the edge on the flap top surface. Downstream, the vortex on the flap side edge grows and eventually merges with the vortex on the flap top surface. Comparison of on- and off-surface flow quantities with our previous experimental measurements shows remarkable agreement. For the 39-deg flap deflection, the calculation also reveals the occurrence of a vortex breakdown, which is corroborated by five-hole probe velocity measurements performed in the Quiet Flow Facility at NASA Langley Research Center. The presence of the vortex breakdown significantly alters the flowfield near the side edge.

Nomenclature

C_p = pressure coefficient
u = streamwise velocity
u^+ = local wall-parallel velocity normalized by inner variables
x = streamwise coordinate
x/c = streamwise coordinate normalized by main chord
x_f/c_f = streamwise coordinate normalized by flap chord, using flap leading edge as origin
y = vertical coordinate
y^+ = wall normal coordinate normalized by inner variables
z = spanwise coordinate
z/c = spanwise coordinate normalized by main chord
α = main airfoil angle of attack
δ_f = nominal flap deflection angle

Introduction

SOUND radiated from the side edge of a partial-span flap is one of the major contributors to airframe noise during aircraft landing. Airframe-generated sound often exposes communities adjacent to major airports to high noise levels by commercial airliners, especially during approach. Current and future Federal Aviation Administration noise regulations make the reduction of airframe noise critical to the continued success of American aircraft manufacturers.

Early work by Ahtye et al.,[1] Fink and Schlinker,[2] and Kendall and Ahtye[3] and recent studies at both NASA Ames Research Center[4] and NASA Langley Research Center[5] all suggest that a significant portion of the airframe noise is generated at the flap side edges. The discussion in Ref. 6 provides an overview of the complex nature of the problem and highlights that, although various models for the flap-side-edge noise have been developed, considerably more work is needed to verify the concepts and develop models with more predictive capability. Such capability is needed because efficient design of modern quiet jetliners requires incorporation of cost-effective noise-prediction tools into the design cycle. The needed improvement in noise prediction for novel configurations necessitates that new semiempirical models be based on flow physics rather than only on empirical correlations. On the other hand, the development of more rigorous models requires a deeper understanding of the local flowfield where noise sources are located.

Based on flow visualizations and surface pressure fluctuation measurements, McInerny et al.[7] conjectured that a dual-vortex system forms in the tip region of a blunt-tipped airfoil. In a series of experiments conducted in the NASA Ames Research Center 7 × 10 ft tunnel (hereafter called 7 × 10), similar conjectures were drawn by Storms et al.[8] for the flap-side-edge flowfield of a generic high-lift system. Using a laser-light-sheet flow-visualization technique, a rough estimate of the location and relative size of the two vortices was obtained. Furthermore, surface static pressure measurements near the side edge also revealed the possible presence of a dual-vortex system. A companion computational effort[9] to the 7 × 10 experiments showed reasonable agreement between the measured and computed surface pressure coefficient away from the flap side edge. Near the side edge, however, the simulation failed to produce the proper pressure coefficient or capture the multiple-vortex flowfield. Very recently, Radeztsky et al.[10] performed extensive on- and off-surface flow measurements of the side-edge flowfield in the NASA Langley Research Center Quiet Flow Facility (QFF). In these measurements the flap-side-edge flowfield was thoroughly mapped, which resulted in the emergence of a clear picture of the local flowfield.

The goal of the present study is to provide an accurate simulation of the flap-side-edge flowfield to corroborate and to complement both the 7 × 10 and QFF experimental databases. Together, the data present a detailed picture of the complex nature of the flap-side-edge flowfield and allow the extraction of the main flow features for noise-source modeling purposes. The results of early calculations were reported by Khorrami et al.[11] Also, computations exclusively tailored to address the QFF experiment's unique setup and features are reported in Ref. 12. The present paper extends the earlier work[11,12] and contains more finely resolved computations, including a vortex breakdown with a 39-deg flap deflection and detailed comparisons with experimental results.

Geometry and Gridding

The model comprises a NACA 63_2-215 Mod B wing with a 30% chord half-span slotted Fowler flap. The main element upstream of the flap includes a trailing-edge cove. The side edge of the flap is flat with sharp edges. More detailed geometrical information is reported in Ref. 8. An overview of the geometry and the coordinate system used in the computation is shown in Fig. 1. For historical reasons, the main-element aspect ratio in the calculations is 2.25

Presented as Paper 98-0768 at the AIAA 36th Aerospace Sciences Meeting, Reno, NV, Jan. 12–15, 1998; received March 11, 1998; revision received Sept. 2, 1998; accepted for publication Sept. 8, 1998.

[*] Senior Scientist, 28 Research Drive. Senior Member AIAA.

[†] Research Scientist; currently Research Scientist, Aeronautic and Acoustic Methods Branch, NASA Langley Research Center, Hampton, VA 23681-2199.

[‡] Research Scientist; currently Assistant Research Professor, Mechanical and Aerospace Engineering Department, Arizona State University, Tempe, AZ 85287. Member AIAA.

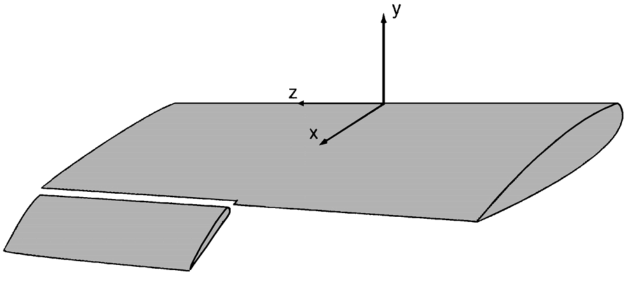

Fig. 1 Simulated model geometry.

rather than the value of 2.0 used in the 7 × 10 experiments. Because the data far from the flap edge are nearly spanwise invariant, the slight differences in span do not influence the important results presented here. All comparisons with experimental data are based on distance from the midspan normalized with the main-element chord. In this work, the angle of attack of the configuration is fixed at 10 deg. Flap deflections of 29 and 39 deg from a nominal retracted position are studied. For all cases, the Reynolds number based on the main-element chord is 3.7×10^6 and the freestream Mach number is 0.2.

The development of grids for the two configurations entailed a series of compromises to balance the need for high-resolution solutions and the practical realities of computing solutions with a large number of grid points. In addition, any gridding strategy chosen had to be amenable to at least three-level multigridding to improve convergence of the solution. The core of the multizone grid topology surrounding the solid surfaces is a modified version of an existing grid used in Refs. 11 and 12.

To simulate the 7 × 10 experiment,[8] the entire test section of the wind tunnel was included in the simulation. Uniform inflow conditions were applied 15 chord lengths upstream of the model. Extrapolation-based outflow conditions were enforced 15 chord lengths aft of the model leading edge. The wind-tunnel walls were modeled as inviscid surfaces to avoid the high computational cost of resolving the wind-tunnel wall boundary layers. All airfoil surfaces were treated as viscous boundaries. The flow domain was divided into 16 separate zones. One-to-one matching of grid points was required at most zone boundaries. For our largest grid, however, to reduce the number of grid points, away from the core zones near the airfoil surfaces patching was used to interpolate solutions across zone boundaries. In all cases where patching was used, the interface surfaces were nearly flat. Although the use of overset gridding techniques can produce a grid with even fewer total grid points, the use of overset grids involves additional computational overhead. In addition, previous studies[9,13] that employed overset grids for this geometry reported difficulties; hence, we opted to employ grids that used a mixture of patching and one-to-one matching of grid points at zone boundaries. Test calculations showed no noticeable differences in the solutions with and without the patched interfaces.

The grid resolution requirements were driven by the need to adequately predict not only surface quantities but also the off-surface dynamics of the local flowfield in the vicinity of the flap side edge. Near the model surfaces, each boundary layer contained 15–25 grid points. Typically, the first grid point from the surface was located less than 10^{-5} chord lengths from the surface. In terms of wall coordinates, the first point off a surface typically had a y^+ of approximately 2. A sample velocity profile on the top surface of the main element at $x/c \approx 0.95$ is shown in Fig. 2. The symbol line represents the computation where the symbols are at the mesh points. Clearly, enough points were packed adjacent to the solid surfaces to resolve the turbulent boundary layer properly. Grid resolution studies were primarily concerned with better resolution of the curved shear layers and vortices adjacent and on top of the flap side edge. Grids with 2.25×10^6 and 3.1×10^6 points were used for the 29-deg flap-deflection case. For the 39-deg deflection case, grids with 3.1×10^6 and 4.45×10^6 points were used. Only changes in the details of the flow near the flap side edge were observed with the different grid resolutions. For instance, in a calculation that used every other grid point in each of the three coordinate directions, we observed only a 3.78% change in the lift coefficient as compared with the lift coefficient obtained for the full 3.1×10^6 point calculation of the 29-deg flap-deflection case. A similar comparison that used every other grid point for the 39-deg flap-deflection case resulted in a 3.81% change in the lift coefficient. The early calculations were performed on the NASA Langley Research Center Cray Y-MP computer. Later computations were performed on the National Aerodynamic Simulation Cray C-90.

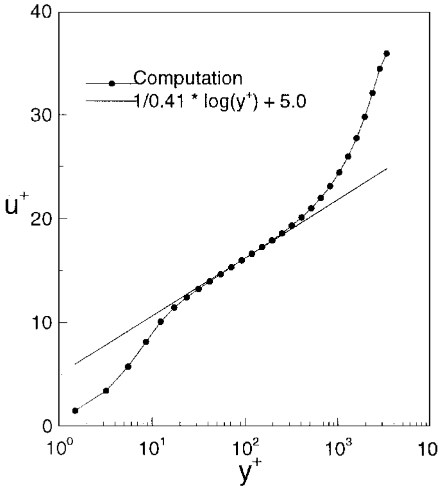

Fig. 2 Sample boundary-layer velocity profile on top surface of main element at $x/c \approx 0.95$.

Flow Solver and Turbulence Model

A standard flow solver, CFL3D,[14–18] was used to compute the flowfield. The computer code CFL3D was developed at NASA Langley Research Center to solve the three-dimensional, time-dependent, thin-layer (in each coordinate direction) Reynolds-averaged Navier–Stokes (RANS) equations using a finite volume formulation. The code uses upwind-biased spatial differencing for the inviscid terms and flux limiting to obtain smooth solutions in the vicinity of shock waves. The viscous derivatives are computed by second-order central differencing. Fluxes at the cell faces are calculated by Roe's flux-difference-splitting method.[19] An implicit three-factor approximate factorization method is used to advance the solution in time. Here, only steady solutions have been computed, and convergence is accelerated with local time stepping, grid sequencing, and multigridding. Patched grid interfaces[20] were used at some grid boundaries to reduce the total number of grid points in the calculation.

The Spalart–Allmaras turbulence model[21] was selected as the turbulence model for all of the results discussed here. The Spalart–Allmaras model is robust, efficient, and tuned to handle general aerodynamic flows, including cases where flow separation and reattachment occur. In the model, the eddy viscosity is directly determined from the solution of a single transport equation. No ambiguous length scales need to be evaluated, as is the case with many previous algebraic and one-equation models. The model has been tested extensively. For high-lift flows, the Spalart–Allmaras model performs about as well as higher-order models[22] and better than algebraic and other one-equation models.[17,22]

Previously, we performed calculations for the 29-deg flap-deflection case using both a k–ε turbulence model and a k–ω turbulence model in addition to the Spalart–Allmaras model.[11] We found the Spalart–Allmaras model to be more efficient in terms of both memory and time requirements, to be more robust, and to produce results that were of comparable quality when compared to experimental results.

Because a turbulent trip near the leading edge was used in the experiments, the calculations were performed with the flow assumed to be fully turbulent from the onset.

Results and Discussion

The presentation of the results is as follows: First, the computed near- and on-surface global results, such as pressure coefficients, are discussed. Direct comparisons with the available experimental measurements are shown. The pressure coefficient C_p plots are followed by a detailed discussion of the computed streamlines on the side edge. Next, an overall picture of the local flowfield at the flap side edge is presented. Finally, attention is focused on the off-surface quantities such as velocity and streamwise vorticity. Once again, direct comparisons with the experimental measurements are provided.

Surface Pressure Coefficient

The pressure coefficients for the 29-deg flap setting were presented in detail in an earlier paper.[11] The computed results showed remarkable agreement with the 7 × 10 measurements across the entire span (both flap and main element). Rather than duplicating those results, we present comparisons with the QFF C_p measurements. The equivalency of the 7 × 10 and QFF flowfields in the vicinity of the flap is discussed by Radeztsky et al.[10] Briefly, because the QFF is an open-jet facility, the presence of the model induces curvature of the jet. To obtain similar pressure distributions on the flap, the main-element angle of attack in the QFF is increased relative to the 7 × 10 experiments. Because the local lift distribution on the flap governs the side-edge-flow phenomena observed there, similar C_p distributions are sufficient to establish nearly identical flow features. The equivalency of the flowfields is reemphasized in Fig. 3, where a sample comparison between the C_p of the QFF, 7 × 10, and the computational fluid dynamics (CFD) is provided. Figure 4 shows the comparison between the computed C_p and the QFF pressure-sensitive paint (PSP) result for the entire flap top surface. The agreement is excellent. All of the relevant flow features are resolved properly. The low-pressure gray strip near the leading edge indicates the acceleration of flow through the gap between the main element and flap. The pear-shape, low-pressure structure at the side edge is the footprint of the side-edge vortex on the flap top surface. Because the vortex rubs against the sharp edge, the lowest pressure peak on the flap occurs inside of this footprint.

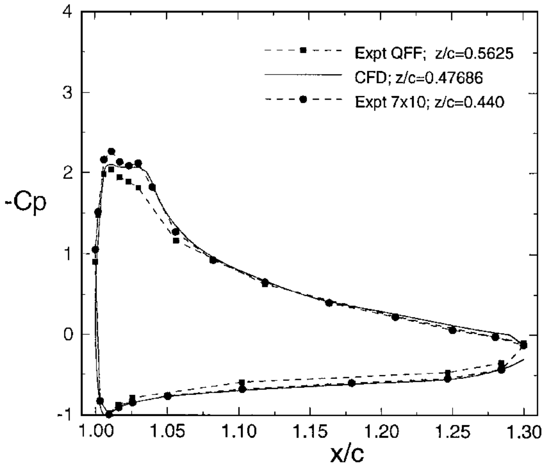

Fig. 3 Comparison of QFF, 7 × 10, and CFD flap C_p for 29-deg deflection.

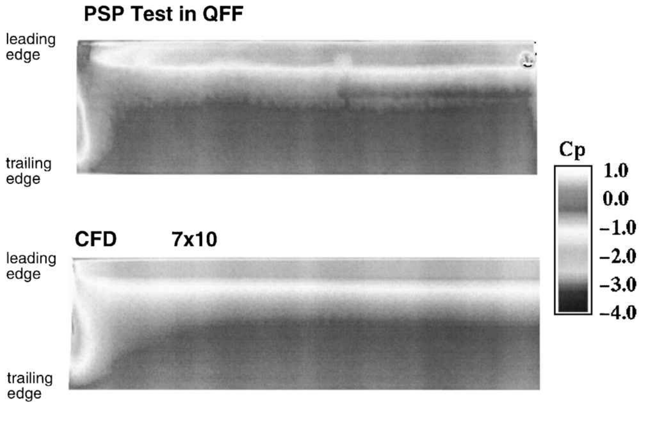

Fig. 4 Comparison between computed C_p and QFF PSP result for entire flap top surface (29-deg deflection).

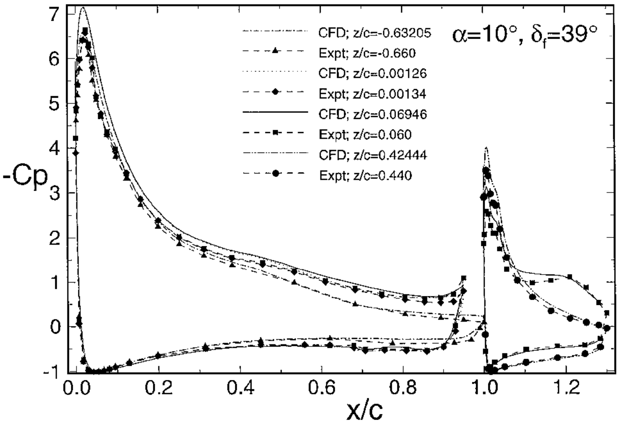

Fig. 5 C_p distribution on both elements at several spanwise locations.

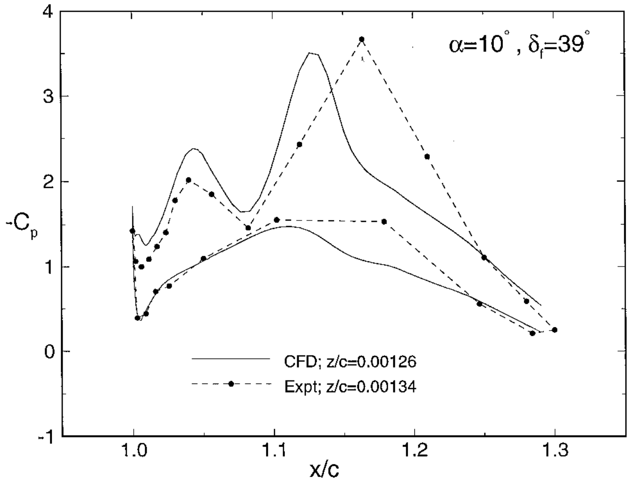

Fig. 6 Flap C_p distribution near side edge.

For the 39-deg flap deflection, the pressure coefficients along the main-element and flap chords at several spanwise locations are shown in Fig. 5. The CFD results show excellent agreement with the 7 × 10 experimental measurements, indicating that the global high-lift behavior is captured properly. The presence of the part-span flap imparts a mild spanwise variation in C_p on the main element. A C_p line plot very close to the flap side edge is shown in Fig. 6. The dual low-pressure peaks, which is a feature of the local flowfield, are captured. Compared to the 7 × 10 measurements, however, the computed results show a higher value for the first peak, and the location of the second peak is shifted upstream slightly. Unfortunately, the density of the pressure ports in the experiment is insufficient to pinpoint the chordwise location of the larger peak.

Side-Edge Surface Streamlines

The computed streamlines on the side edge for the 29-deg flap deflection were previously discussed by Khorrami et al.[11] Here we present results for the 39-deg case only. The near-wall streamlines restricted to the plane one grid point above the solid surface are shown in Fig. 7. These streamlines are in excellent agreement with the QFF surface oil-flow patterns on the flap side edge that are discussed by Radeztsky et al.[10] Because of the sharp corner, the primary separation line is affixed to the bottom edge. The presence of the primary attachment line is very well captured in the computation. This line begins near the leading edge and moves toward the upper surface, becoming nearly tangent to it about a third of the flap chord downstream. Eventually, the attachment line turns toward the lower edge beyond the midflap region. The computed streamlines also capture the formation and location of the secondary attachment and separation lines. Both of these lines, which are situated near the bottom edge and run parallel to it, abruptly end in the vicinity of a focal point. Downstream of this point, the flow is reversed and moves

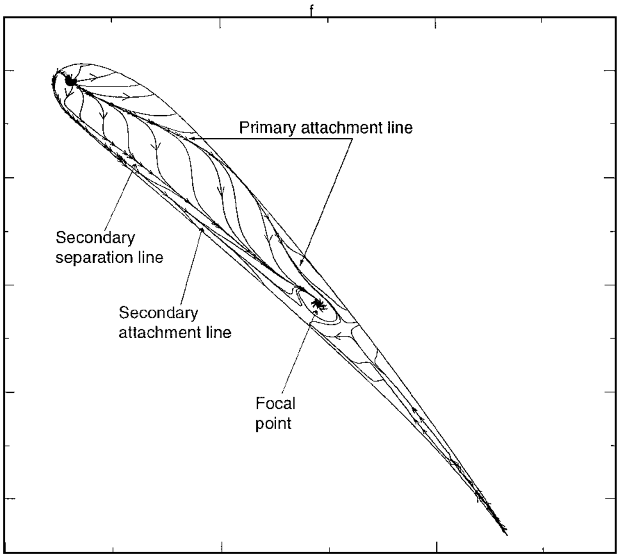

Fig. 7 Flap-side-edge near-surface streamlines (39-deg deflection).

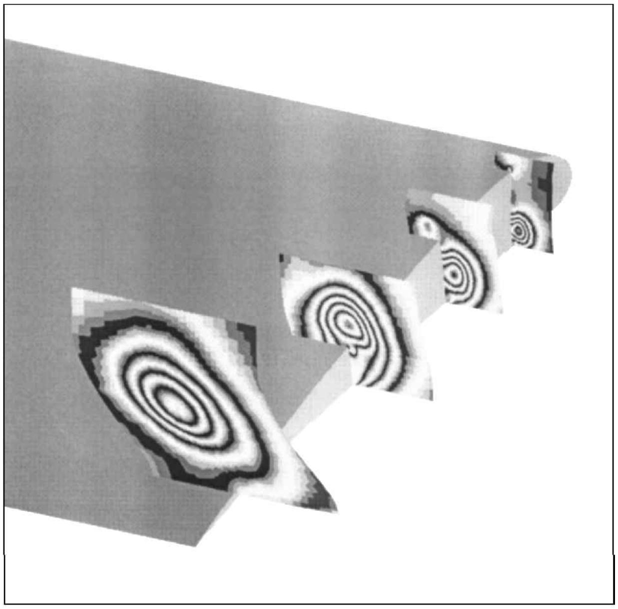

Fig. 8 Flap static pressure field showing dual-vortex system at side edge (29-deg deflection).

upstream. The surface oil-flow pattern from the NASA Langley Research Center QFF experiment showed accumulation of oil at a similar point. This observation was puzzling and initially unexplainable. Not until the computed streamlines revealed the presence of this focal point and the reversed flow downstream of it did a clear understanding of the side-edge streamlines emerge.

Side-Edge Flowfield General Features

Before presenting detailed quantitative comparisons, a brief overview of the relevant flow features at the side edge is provided.

An effective technique for visualizing the embedded vortical structures within the side-edge flowfield is via display of the static pressure field. Depending on the strength of a vortex, the centrifugal force field establishes a strong radial pressure gradient, with the vortex core having the minimum pressure. To display the location of the vortices in a black-and-white figure, we decided to show the static pressure in a zebra format. In this format, light and dark fringes indicate changes in the pressure contour. Although no quantitative information should be deduced from these figures, regions of local extrema and the local gradients are easily seen. The static pressure field for the 29-deg flap deflection, in essentially y–z planes at four streamwise locations, is shown in Fig. 8. The normalized pressure range used in Figs. 8 and 9 is between 0.6 and 0.72, with the freestream pressure of approximately 0.714. Figure 8 clearly shows that a dual-vortex system is established near the flap leading edge. The primary vortex is formed near the bottom edge and rapidly grows in size in the streamwise direction until it occupies the entire side edge. The weaker vortex is formed on the suction surface at the side edge and only grows moderately in size as it moves in the streamwise direction.

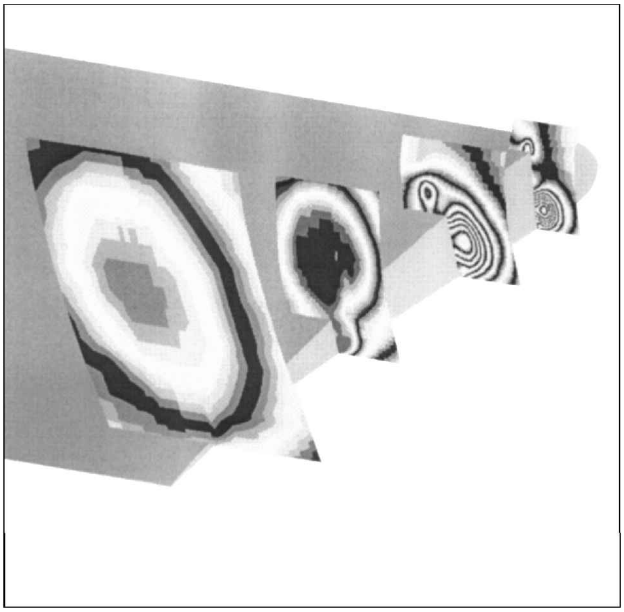

Fig. 9 Flap static pressure field showing dual vortex system at side edge (39-deg deflection).

At a station near the flap midchord, the primary vortex is detached from the side edge, moves on top, and merges with the top vortex to form a single strong vortex. The concentric fringes in the last two planes are evidence of an organized vortex-core structure. Further interrogation of the computational database revealed that the separated shear layer at the bottom edge is a constant source of vorticity that gets wrapped around the vortex and feeds it. This constant feeding results in a stronger vortex with a low-pressure core causing the axial velocity in the core to attain a speed up to twice the freestream speed.

The static pressure field for the 39-deg case is shown in Fig. 9. Near the flap leading edge, a pattern very similar to the case of the 29-deg deflection is established. The higher number of fringes in the cores, however, is indicative of the existence of larger radial pressure gradients in both vortices. Unlike the 29-deg case, immediately after the merging of the two vortices, in the 39-deg case, the postmerged vortex displays a disorganized core consisting mostly of constant pressure fluid.

Vortex Breakdown

The disorganized core, for the 39-deg flap deflection, suggests the occurrence of vortex breakdown. This phenomenon is corroborated by five-hole probe velocity measurements performed in the QFF. The postmerged vortex core has expanded, and its axial velocity has rapidly decelerated, eventually forming a region of flow reversal. Figure 10a shows the vortex-breakdown flowfield in the vicinity of the flap side edge. The ribbons represent the flow streamlines at and near the flap side edge. For clarity only the flap geometry is displayed. Near the flap trailing edge, the darkest region, in the shape of a bubble, shows the spatial extent of the axial flow reversal region. Beyond the bubble region, the core axial velocity reaccelerates and is directed downstream. We emphasize that the use of bubble terminology here is based purely on appearances in Fig. 10a. The ribbons also display the locations of the two vortices near the flap side edge and their subsequent merging upstream of the breakdown region. This work represents the first time that vortex breakdown has been reported to be numerically computed in a multielement high-lift configuration. Most prior calculations did not

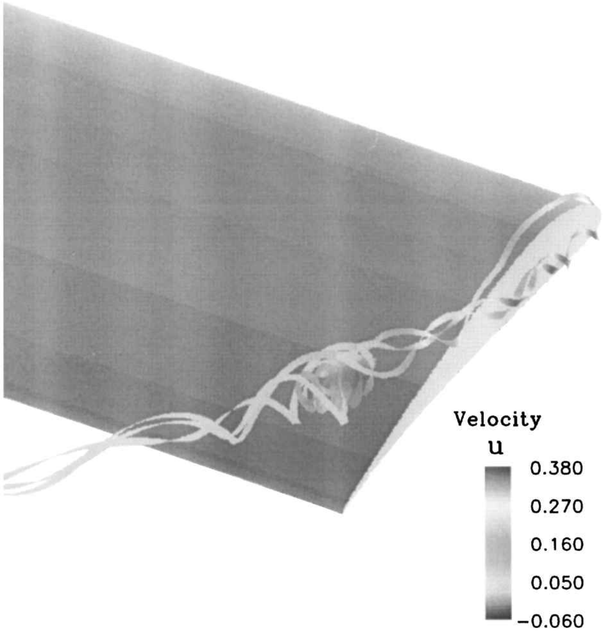

Fig. 10a Streamlines identifying vortex breakdown region near flap side edge (39-deg deflection); velocity scale is with respect to sound speed, i.e., freestream value is 0.2.

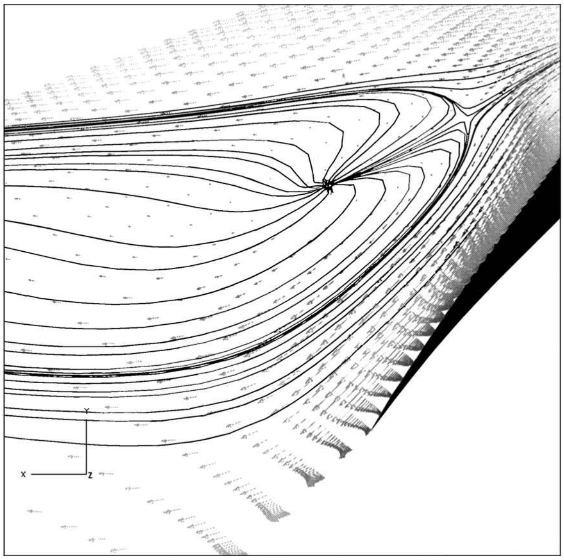

Fig. 10b Vortex breakdown region identified by flow streamlines and vectors projected onto *x–y* plane at flap side edge.

provide sufficient grid resolution in the vicinity of the vortices and did not interrogate the data as thoroughly as was done here. In addition, without corresponding experimental results, computational results suggesting vortex breakdown in a multielement high-lift configuration would have been viewed suspiciously.

In some regards, the present vortex breakdown is quite dissimilar to the classical bubble-type or the spiral-type breakdowns that one observes in a tube. Figure 10b shows the projected vectors and the flow streamlines onto the x–y plane that corresponds to the spanwise location of the side-edge surface. In Fig. 10b, the aft midchord part of the flap side edge is shown as a black surface. Whereas the streamlines show the expected rapid expansion of the vortex core ahead of the breakdown point, the behavior of the streamlines in the internal region of the breakdown markedly deviates from the observed breakdown phenomena in axisymmetric tubes. Rather than internal recirculating zones, an apparent focal point exists to which all of the streamlines converge. In three dimensions, the apparent focus is actually a saddle point. Fluid is brought to the saddle point in this two-dimensional cut but moves away from the saddle point in the out-of-plane directions. Near the tip of the breakdown region, the dividing streamlines have a parabolic shape that is typical for vortex-breakdown regions, but farther aft the dividing streamlines develop an elongated shape that resembles a banana. The time-averaged internal structure of the vortex breakdown at this spanwise location has been confirmed by C.-S. Yao via particle image velocimetry (PIV) measurements performed at NASA Langley Research Center. An initial sample of PIV measurements is presented by Macaraeg.[23] However, because the actual internal structure is unsteady, the time-averaged data are not appropriate for discerning the true internal structure of the vortex breakdown.

Off-Surface Quantities

Off-surface measurements of velocity in the QFF experiment were obtained with a five-hole probe.[10] The experimental resolution of the velocity data was sufficiently fine for spatial derivatives of the velocity field to provide smooth vorticity contours. Depending on the local flow conditions, probe data were obtained on grids with point spacings ranging from 0.5 to 2.0 mm. The 1.59-mm diameter of the five-hole probe limited the closest approach to the flap surface. The estimated error of the five-hole probe varies greatly in a strong vortex. Based on the work of Kjelgaard,[24] Radeztsky et al.[10] estimate the error in the velocity components at less than 5% in regions where the velocity gradients are less than 800 s^{-1}. Much larger errors are expected in regions with higher velocity gradients. Because of the enormous volume of information available, only streamwise vorticity and axial velocity contours at selected locations are chosen for direct comparison with the experimental results. The experimental data were obtained in planes oriented approximately perpendicular to the flap chord line.

29-Degree Case

Figure 11 shows the position of the planes for the 29-deg flap deflection. The planar CFD cuts are made at angles and locations that correspond to these experimental planes.[10] The selected locations along the side edge are at $x_f / c_f \approx 0.18$, 0.51, and 0.84 from the leading edge of the flap.

The computed axial vorticity contours at $x_f / c_f \approx 0.18$ are shown in Fig. 12a. The dual-vortex system forms early, not too far from the flap leading edge. The vortex residing near the bottom edge is bigger and stronger relative to the top vortex. Although somewhat difficult to see, the curved shear layers that feed vorticity into these vortices are also resolved. These shear layers are formed in response to boundary-layer separation at both bottom and top sharp corners. The corresponding experimental data are plotted in Fig. 12b. Note that the experimental planes do not extend all of the way to the solid surfaces because of the measuring probe's finite size. In addition, the small white square region in the flowfield is caused by the discarding of the measured data wherever the range of validity of the five-hole probe is violated. The agreement between measurements and predictions is quite good, which shows that the relevant flow features are captured appropriately.

The computed axial vorticity contours near the midflap section are presented in Fig. 13a. At this location, the side vortex has grown

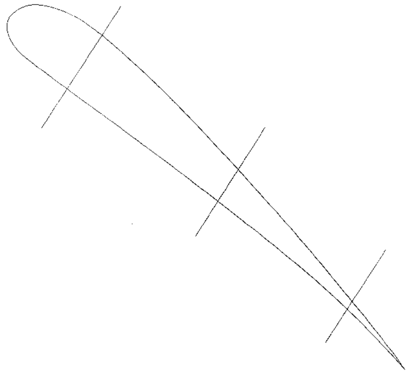

Fig. 11 Locations of selected planes for comparing off-surface quantities (29-deg case).

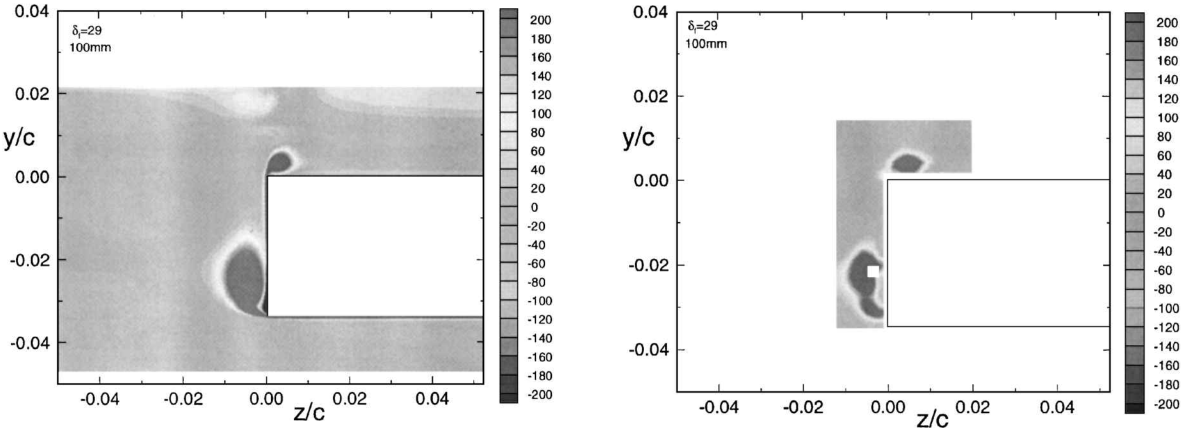

a) CFD

b) Experiment

Fig. 12 Axial vorticity contours at $x_f/c_f \approx 0.18$ (29-deg case).

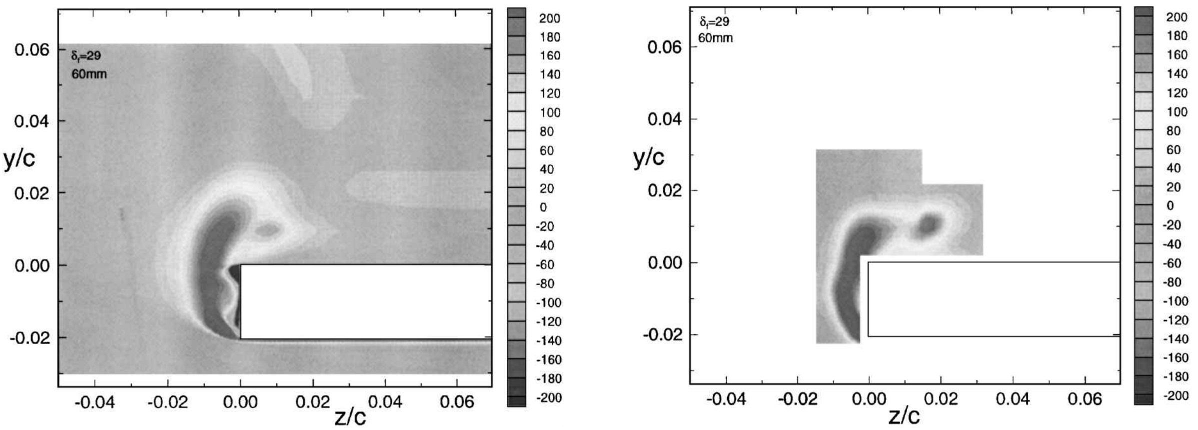

a) CFD

b) Experiment

Fig. 13 Axial vorticity contours at $x_f/c_f \approx 0.51$ (29-deg case).

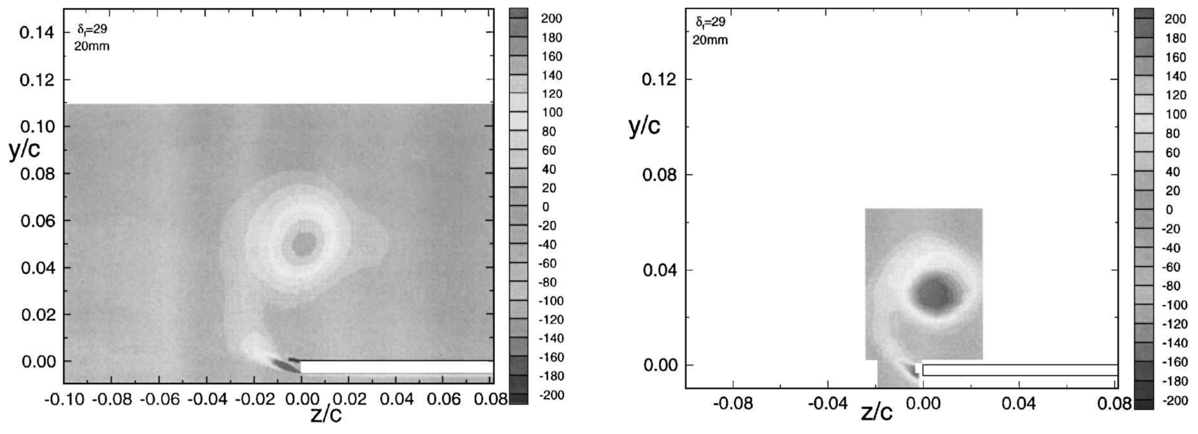

a) CFD

b) Experiment

Fig. 14 Axial vorticity contours at $x_f/c_f \approx 0.84$ (29-deg case).

in size and strength and is in the process of moving onto the flap top surface. At the same time, the side vortex is starting to influence and interact with the smaller top vortex. A strong curved shear layer, emanating from the bottom edge, feeds vorticity into the side-edge vortex. The computed flowfield in the midsection of the flap is very well corroborated by the experimentally measured contours shown in Fig. 13b. These contours plus the volumetric database have been used to develop an idealized model of the curved shear layer at the side edge. The preliminary results of Khorrami and Singer[25] that are based on this idealized model of the shear layer suggest that instabilities that grow in the shear layer are leading candidates to be strong noise sources at the flap side edge. In addition, the steady RANS planar cuts are being used as the base flow for two-dimensional direct numerical simulations[26] to locate the local regions where unsteady features are supported. The initial results are quite informative and suggest that the side-edge flowfield is capable of supporting a broad band of flow unsteadiness.

Near the flap trailing edge, the computed vorticity field shows that the two vortices have merged and a single-dominant, nearly axisymmetric vortex is created (Fig. 14a). These contours compare very well with the measured contours shown in Fig. 14b. A comparison of the axial velocity distribution across the vortex core is

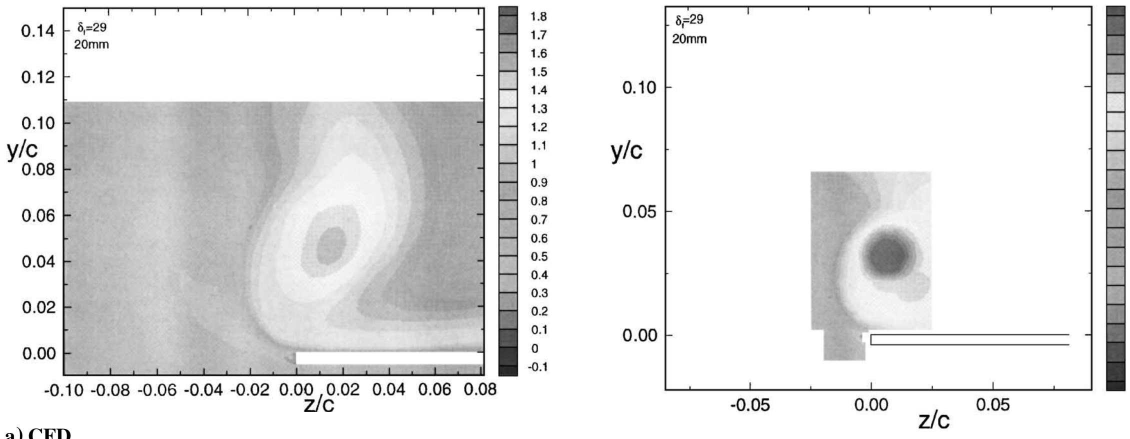

a) CFD

b) Experiment

Fig. 15 Axial velocity contours at $x_f/c_f \approx 0.84$ (29-deg case).

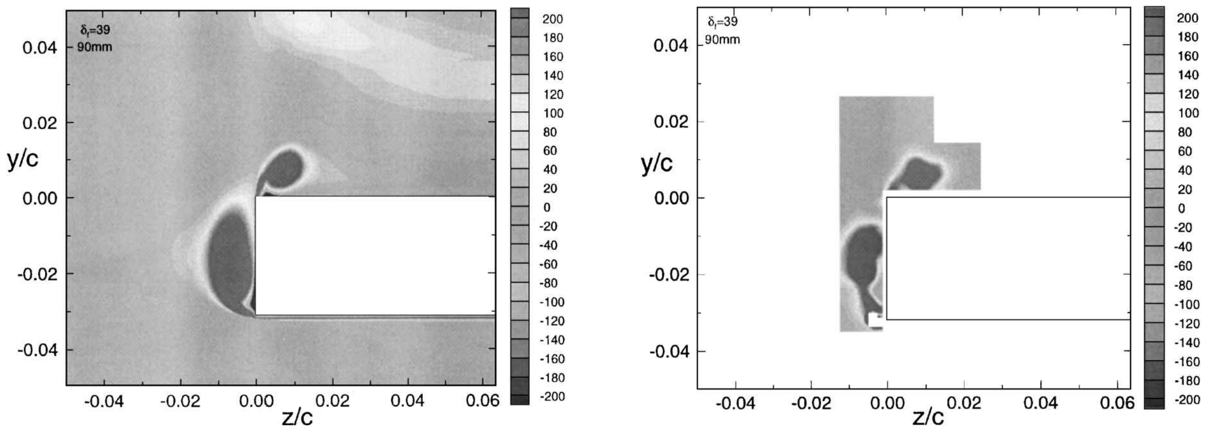

a) CFD

b) Experiment

Fig. 16 Axial vorticity contours at $x_f/c_f \approx 0.26$ (39-deg case).

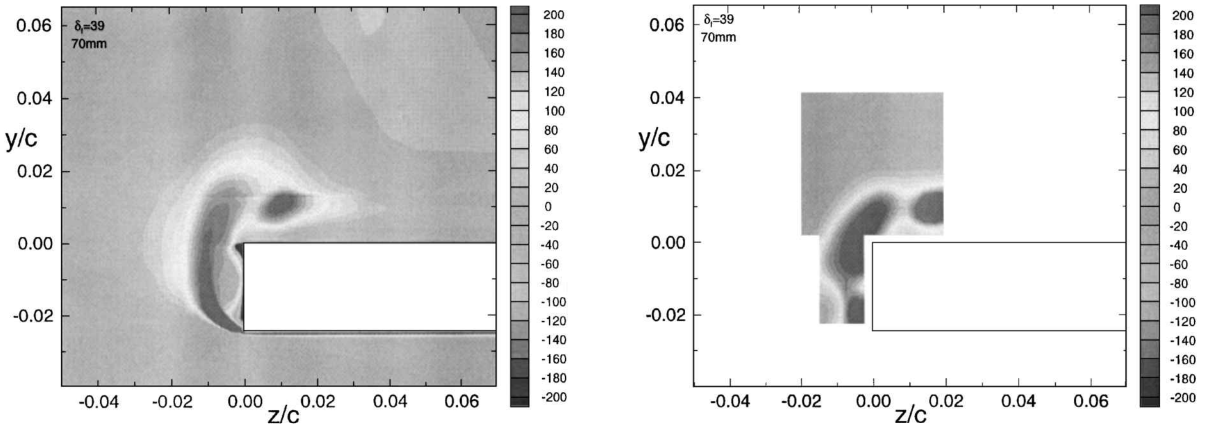

a) CFD

b) Experiment

Fig. 17 Axial vorticity contours at $x_f/c_f \approx 0.43$ (39-deg case).

shown in Figs. 15a and 15b. The CFD results show a core at this location with velocity in excess of 1.7 times the freestream velocity. The measured contours show even higher values, reaching nearly twice the freestream velocity. Although the comparison between CFD and experiment in Figs. 14 and 15 is in excellent agreement qualitatively, quantitatively some minor differences exist. First, the computation underpredicts streamwise vorticity and axial velocity by 10–15% relative to the measurements. Second, the simulated vortex core resides somewhat higher from the flap top surface. Both of these differences are attributed to a lack of grid resolution away from solid surfaces, although turbulence modeling issues may also play a part.

39-Degree Case

As in the 29-deg case, the off-surface quantities are presented at only three locations along the flap side edge. The selected positions are $x_f/c_f \approx 0.26$, 0.43, and 0.84. Once again, the planar cuts through the volumetric CFD database were chosen to coincide with the experimental planes where measurements were made.

The computed and measured vorticity contours at $x_f/c_f \approx 0.26$ are shown in Figs. 16a and 16b, respectively. The presence of a dual-vortex system at the flap side edge is clearly demonstrated. Except for a slightly larger side vortex in the calculation, Figs. 16a and 16b are in good agreement, both qualitatively and quantitatively. Because of a higher flap deflection, these vortices are stronger and

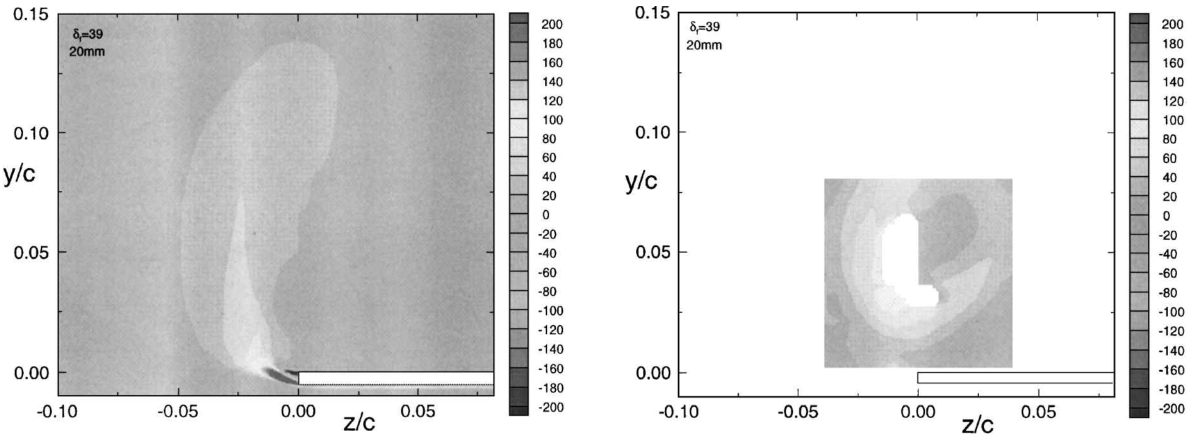

a) CFD

b) Experiment

Fig. 18 Axial vorticity contours at $x_f/c_f \approx 0.84$ (39-deg case).

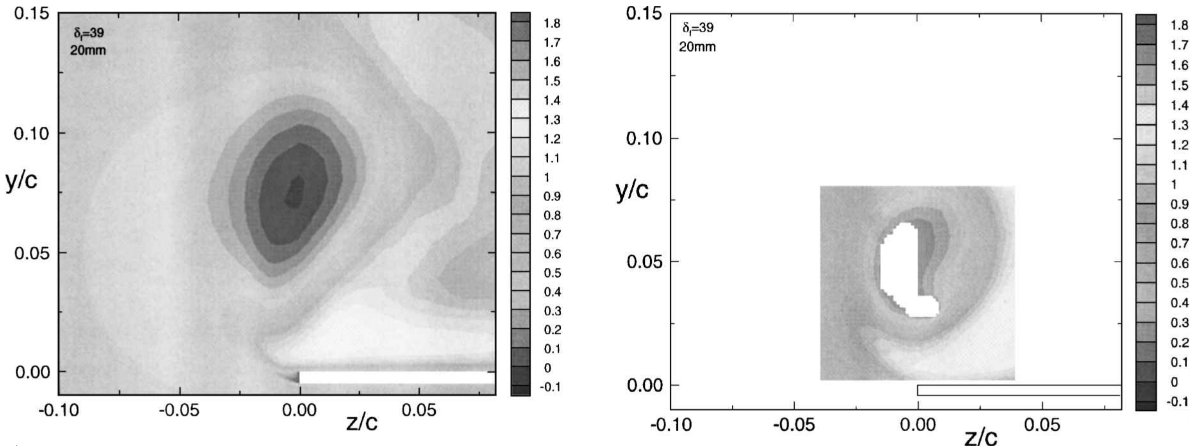

a) CFD

b) Experiment

Fig. 19 Axial velocity contours at $x_f/c_f \approx 0.84$ (39-deg case).

larger when compared to the 29-deg case at a comparable location. Figures 16a and 16b also show the spatial position and thickness of the two shear layers emanating from the sharp corners. The accumulation of opposite-sign vorticity beneath the vortices close to the edges in Fig. 16a indicates secondary separation.

Figures 17a and 17b show the axial vorticity field near the flap midsection. Once again, the agreement between measurements and predictions is remarkable. At this location, the side vortex has moved upward and is starting to affect the top vortex. The vortex passes very close to the top edge, causing a strong interaction, as is evident by the accumulation of opposite-sign vorticity on the side near the edge. In addition, the spatial position and the strength of the curved shear layer, which feeds vorticity into the side vortex, is displayed effectively. One point of concern for the CFD is the thickness of the shear layer, which seems to be a bit large. Although a considerable number of grid points are packed near the side edge, to fully resolve the shear layer one must do even better.

Figure 18a presents vorticity contours near the flap trailing edge of the computed postmerged vortex. As expected, the vortex breakdown diffuses the streamwise vorticity. The CFD results are corroborated by the measured field, which shows that the core vorticity is diffused over a large area (Fig. 18b). As indicated earlier, the white cut-out region in the middle of the measurement plane shows where the five-hole probe's range of validity was violated. The extent of the flow reversal region in the vortex core is shown in Fig. 19a, where the computed axial velocity contours are shown. According to the computations, the maximum reverse flow in the breakdown region achieves a value close to 10% of the freestream velocity. A comparison with the measured axial velocity field (Fig. 19b) shows the overall flow features to be in good agreement. Unfortunately, the five-hole probe is incapable of providing the magnitude of the reversed flow.

The general agreement of the CFD results and the five-hole probe measurements eliminated early concerns that the finite size of the five-hole probe induced the vortex breakdown.

Conclusion

Steady RANS calculations of a high-lift airfoil with a half-span flap were performed for 29- and 39-deg flap deflections. The computed results are in excellent agreement with the companion experimental measurements revealing the complex nature of the vortex system at the side edge. At the higher deflection, the computations accurately capture the occurrence and location of vortex breakdown near the side edge.

The present computations clearly show that, given the proper care (grid distribution, postprocessing, etc.), the CFD analysis can be used as a routine diagnostic tool on a fairly complex three-dimensional flowfield. In fact, during the course of the present study, on several occasions, the computed results directed subsequent experimental measurements to be focused on a particular region of interest. The usefulness of the volumetric CFD database goes far beyond the comparison attempted in this paper and a mere corroboration of the experimental measurements. The wealth of information provided by the CFD database has given us insight into the nature of the flow physics at the flap side edge and has allowed us to design tip modifications to alter the flowfield for noise reduction purposes. In addition, the computed result currently is being utilized to construct idealized flow models and to develop appropriate noise-prediction tools.

Acknowledgments

This work was partially sponsored by NASA Contracts NAS1-20059 and NAS1-20103 (McDonnell Douglas Subcontract MDA-HTC-20103-23). Most of the calculations were performed on computers provided by the National Aerodynamic Simulation Facility. The authors would like to thank C.-S. Yao for the particle image velocity measurements performed at NASA Langley Research Center. The authors would also like to thank members of the Airframe Noise Team at NASA Langley Research Center for many helpful discussions. Especially helpful was Mamad Takallu of Lockheed Martin Engineering and Sciences Company, who shared with us the initial version of the grid and input files. The assistance of Michael R. Wiese of Computer Sciences Corporation, who painstakingly incorporated numerous grid modifications, is also greatly appreciated.

References

[1] Ahtye, W. F., Miller, W. R., and Meecham, W. C., "Wing and Flap Noise Measured by Near- and Far-Field Cross-Correlation Techniques," AIAA Paper 79-0667, March 1979.

[2] Fink, M. R., and Schlinker, R. H., "Airframe Noise Component Interaction Studies," AIAA Paper 79-0668, March 1979.

[3] Kendall, J. M., and Ahtye, W. F., "Noise Generation by a Lifting Wing/Flap Combination at Reynolds Numbers to 2.8×10^6," AIAA Paper 80-0035, Jan. 1980.

[4] Hayes, J. A., Horne, W. C., Soderman, P. T., and Bent, P. H., "Airframe Noise Characteristics of a 4.7% Scale DC-10 Model," AIAA Paper 97-1594, May 1997.

[5] Meadows, K. R., Brooks, T. F., Humphreys, W. M., Hunter, W. H., and Gerhold, C. H., "Aeroacoustic Measurements of a Wing-Flap Configuration," AIAA Paper 97-1595, May 1997.

[6] Crighton, D., "Airframe Noise," *Aeroacoustics of Flight Vehicles: Theory and Practice*, NASA Reference Publication 1258, Vol. 1, WRDC TR 90-3052, Aug. 1991.

[7] McInerny, S. A., Meecham, W. C., and Soderman, P. T., "Pressure Fluctuations in the Tip Region of a Blunt-Tipped Airfoil," *AIAA Journal*, Vol. 28, No. 1, 1990, pp. 6–13.

[8] Storms, B. L., Takahashi, T. T., and Ross, J. C., "Aerodynamic Influence of a Finite-Span Flap on a Simple Wing," Society of Automotive Engineers, SAE Paper 951977, Los Angeles, CA, Sept. 1995.

[9] Mathias, D. L., Roth, K. R., Ross, J. C., Rogers, S. E., and Cummings, R. M., "Navier–Stokes Analysis of the Flow About a Flap Edge," AIAA Paper 95-0185, Jan. 1995.

[10] Radeztsky, R. H., Singer, B. A., and Khorrami, M. R., "Detailed Measurements of a Flap Side-Edge Flow Field," AIAA Paper 98-0700, Jan. 1998.

[11] Khorrami, M. R., Singer, B. A., and Takallu, M. A., "Analysis of Flap Side-Edge Flow Field for Identification and Modeling of Possible Noise Sources," Society of Automotive Engineers, SAE Paper 971917, Traverse City, MI, May 1997.

[12] Takallu, M. A., and Laflin, K. R., "Reynolds-Averaged Navier–Stokes Simulations of Two Partial-Span Flap Wing Experiments," AIAA Paper 98-0701, Jan. 1998.

[13] Mathias, D. L., and Cummings, R. M., "Numerical Design of Advanced Multi-Element Airfoils," NASA Cooperative Agreement NCC-2-813 Final Rept., California Polytechnic State Univ., San Luis Obispo, CA, Oct. 1994.

[14] Thomas, J., Krist, S., and Anderson, W., "Navier–Stokes Computations of Vortical Flows over Low Aspect-Ratio Wings," *AIAA Journal*, Vol. 28, No. 2, 1990, pp. 205–212.

[15] Vatsa, V. N., Thomas, J. L., and Wedan, B. W., "Navier–Stokes Computations of Prolate Spheroids at Angle of Attack," *Journal of Aircraft*, Vol. 26, No. 11, 1989, pp. 986–993.

[16] Thomas, J. L., "Reynolds Number Effects on Supersonic Asymmetrical Flows over a Cone," *Journal of Aircraft*, Vol. 30, No. 4, 1993, pp. 488–495.

[17] Rumsey, C. L., Sanetrik, M. D., Biedron, R. T., Melson, N. D., and Parlette, E. B., "Efficiency and Accuracy of Time-Accurate Turbulent Navier–Stokes Computations," *Computers and Fluids*, Vol. 25, No. 2, 1996, pp. 217–236.

[18] Rumsey, C. L., Gatski, T. B., Ying, S. X., and Bertelrud, A., "Prediction of High-Lift Flows Using Turbulent Closure Models," AIAA Paper 97-2260, June 1997.

[19] Roe, P., "Approximate Riemann Solvers, Parameter Vectors, and Difference Schemes," *Journal of Computational Physics*, Vol. 43, Oct. 1981, pp. 357–372.

[20] Biedron, R. T., and Thomas, J. L., "A Generalized Patched-Grid Algorithm with Application to the F-18 Forebody with Actuated Control Strake," *Computing Systems in Engineering*, Vol. 1, Nos. 2–4, 1990, pp. 563–576.

[21] Spalart, P. R., and Allmaras, S. R., "A One-Equation Turbulence Model for Aerodynamic Flows," AIAA Paper 92-0439, Jan. 1992.

[22] Rogers, S. W., Menter, F. R., Durbin, P. A., and Mansour, N. N., "A Comparison of Turbulence Models in Computing Multi-Element Airfoil Flows," AIAA Paper 94-0291, Jan. 1994.

[23] Macaraeg, M. G., "Fundamental Investigations of Airframe Noise," AIAA Paper 98-2224, June 1998.

[24] Kjelgaard, S. O., "Theoretical Derivation and Calculation Technique of a Hemispherical-Tipped Five Hole Probe," NASA TM-4047, Dec. 1988.

[25] Khorrami, M. R., and Singer, B. A., "Stability Analysis for Noise-Source Modeling of a Part-Span Flap," AIAA Paper 98-2225, June 1998.

[26] Streett, C. L., "Numerical Simulation of Fluctuations Leading to Noise in a Flap-Edge Flowfield," AIAA Paper 98-0628, Jan. 1998.

J. P. Gore
Associate Editor